

Identification of Flight Dynamics of a Cyclocopter Micro Air Vehicle in Hover

Vikram Hrishikeshavan,* Moble Benedict,[†] and Inderjit Chopra[‡]
University of Maryland, College Park, Maryland 20783

DOI: 10.2514/1.C032633

This paper discusses the control methodology, flight dynamics identification, and disturbance rejection analysis in hover of a revolutionary horizontal-axis rotary-wing concept: the twin cyclocopter. The vehicle has a gross weight of 500 g (1.25 by 1.67 by 1 ft in dimensions) and comprises two highly optimized cyclorotors along with a tail rotor for pitch control. Stable hover flight required fast control of the rpm and thrust vectoring of the rotors through onboard feedback regulation. A six-degree-of-freedom flight dynamics model of the vehicle was extracted through input excitation and time-domain identification. The longitudinal and heave degrees of freedom were decoupled and independent from the rest of the dynamics. Longitudinal translation damping was higher than in the heave mode, indicating differences in restoring forces at different blade azimuth positions due to the different pitch angles. Strong gyroscopic coupling was observed between lateral and yaw degrees of freedom because the rotors spin in the same direction, resulting in unbalanced angular momentum, which is an important characteristic of the twin cyclocopter. Coupling between lateral velocity perturbation and yaw response was also observed. Analysis based on a control-theoretic framework indicated sufficient maneuverability potential of the vehicle in open-loop condition. The longitudinal and lateral gust tolerances were calculated to be about 7.9 and 17 m/s, respectively.

I. Introduction

DURING the past decade, there have been significant research accomplishments toward the development of efficient micro air vehicles (MAVs) [1,2] due to their potential to support tactical situational awareness in military missions and many other applications that may be dangerous or cumbersome for human involvement. There is a need to develop platforms with improved fidelity and capability to operate in confined spaces and tolerate external aerodynamic disturbances such as wind gusts and flow recirculation due to ground effects, while also exhibiting good aerodynamic performance. Many missions would require a high level of maneuverability and gust tolerance (Fig. 1). A number of conventional rotor configurations such as single, coaxial, and multirotors have been developed. However, a significant limitation for operation at these scales is the reduced aerodynamic efficiency due to the low-Reynolds-number flow regimes [3]. Therefore, novel vehicle configurations such as a cycloidal rotor concept should be explored. Systematic experimental studies [4,5] have shown that cyclorotors can have improved aerodynamic performance over conventional rotors for a wide range of flight conditions (Fig. 2). In addition to the hover performance, it is important to characterize the flight dynamics of the cyclocopter to enable a wider scope for comparison with other platforms as well as implementation of model-based controllers for optimal and robust control.

Previous attempts to build a flight-capable cyclocopter have been going on from the early 20th century [6,7]. Almost all of these vehicles were at full scales, such as the “wheeled orthopter” built in 1909 and the Rahn cyclogyro built in 1935 (Fig. 3). None of these attempts, however, was successful in achieving flight due to the high structural loads at large scales and lack of understanding of basic performance and design tools. However, with the recent break-

throughs in fabrication techniques, high-energy-density propulsion systems, and experimental optimization, it has been possible to develop flight-capable cyclocopters today [8–10]. Figure 4 shows the various flying cyclocopter MAVs developed at the University of Maryland. With the successful demonstration of flightworthiness of the concept demonstrated, it now becomes necessary to characterize the flight dynamics of the vehicle to enable comparisons with more established conventional rotor MAV platforms.

A reduced-order flight dynamic model of the cyclocopter can be experimentally determined about the hover condition through systematic system-identification techniques. To assess the inherent maneuverability potential as well as the vehicle’s susceptibility to gust disturbances, control design tools can be implemented based on the identified flight dynamics model. These tools quantitatively identify the inherent vehicle characteristics, which are independent of any control algorithm. This analysis has been developed and applied to stable [11] and unstable systems [12].

The objective of the paper is to systematically characterize the bare airframe dynamics of the cyclocopter in hover. This would enable quantification of the maneuverability and gust rejection capability of the vehicle and establish a framework for comparison with other MAV platforms. The cyclorotor concept, vehicle design, and hover-flight testing are initially described. The methodology and results from the system-identification experiments are then detailed. Finally, quantification of the maneuverability and gust-tolerance metrics are discussed.

II. Cycloidal Rotor Concept for Micro Air Vehicle

A cycloidal rotor is a rotating-wing system where the span of the blades runs parallel to the axis of its rotation, as shown in Fig. 5. In hover, the pitch angle of each blade is varied in a cyclic manner by mechanical means such that the blade experiences positive pitch angles at both the top and bottom positions of the azimuth cycle. The resulting time-varying lift and drag forces produced by each blade are resolved into the vertical and horizontal directions, as shown in Fig. 6. By varying the phase and amplitude of the blade pitch, the magnitude and direction of the net thrust vector produced by the cyclorotor can be controlled. Because each spanwise blade element of a cyclorotor operates at similar aerodynamic conditions (same angle of incidence, flow velocity), the blades can be designed for maximum aerodynamic efficiency. Previous studies at the University of Maryland have shown that the aerodynamic efficiencies of cyclorotors can be greater than those of conventional rotor systems. A further advantage with a

Received 16 September 2013; revision received 16 January 2014; accepted for publication 19 January 2014; published online 29 April 2014. Copyright © 2014 by the American Institute of Aeronautics and Astronautics, Inc. All rights reserved. Copies of this paper may be made for personal or internal use, on condition that the copier pay the \$10.00 per-copy fee to the Copyright Clearance Center, Inc., 222 Rosewood Drive, Danvers, MA 01923; include the code 1542-3868/14 and \$10.00 in correspondence with the CCC.

*Assistant Research Scientist, Department of Aerospace Engineering; vikramh@umd.edu. Member AIAA.

[†]Asistant Research Scientist, Department of Aerospace Engineering; moble@umd.edu. Member AIAA.

[‡]Alfred Gessow Professor and Director; chopra@umd.edu. Fellow AIAA.

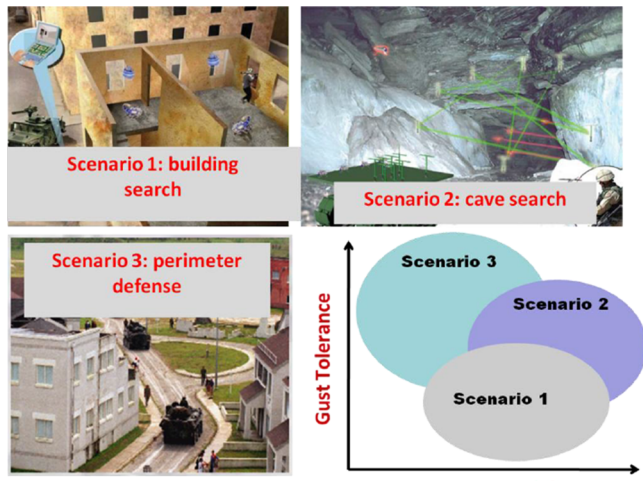


Fig. 1 Examples of MAV operations in aerial surveillance missions with different requirements of gust tolerance and maneuverability.

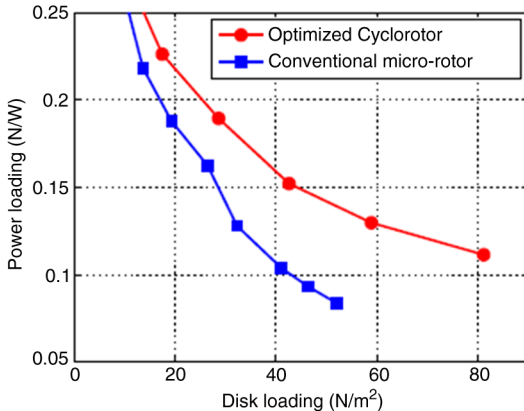


Fig. 2 Power loading for optimized cyclorotor compared with conventional microrotor [4].



Fig. 3 Previously developed cyclogyro prototypes.

cyclorotor-based MAV is that the direction of the thrust vector can be changed almost instantaneously in any direction. This may have implications on the gust rejection capability of the vehicle, which will be explored further in this paper. One major drawback of a cyclorotor is its relatively large rotating structure. Therefore, to reduce the rotor weight, careful design of the cyclorotor is required.

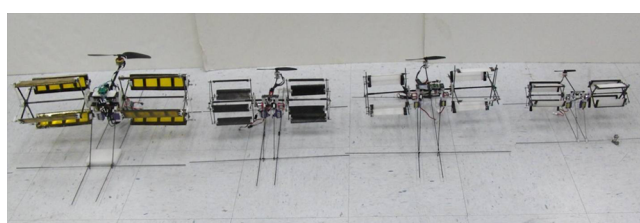


Fig. 4 Flight-capable cyclocopters developed at the University of Maryland, representing models with gross weight of 500, 200, and 100 g, respectively.

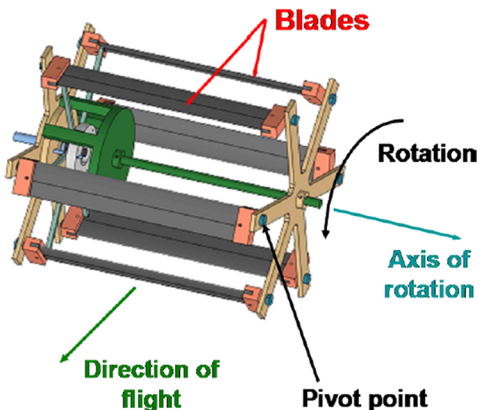


Fig. 5 Cycloidal rotor.

III. Vehicle Design and Integration

In this paper, a twin-rotor cyclocopter is considered as shown in Fig. 7. It consists of two cycloidal rotors spinning in the same direction, with the blades on the top advancing forward. This creates an unbalanced nose-up pitching moment. To counteract this, a tail rotor is incorporated, which thrusts upward. The vehicle measures approximately 1.25 ft in length, 1.67 ft in breadth, and 1 ft in height. The gross weight of the vehicle including the battery is 500 g. The cycloidal rotor has a diameter of 6 in. and a blade chord of 2 in. Each rotor is driven independently by a 75 W outrunner motor through a single-stage 7.5:1 transmission. Each cyclorotor produces more than 200 g of thrust, consuming close to 60 W of electrical power. The tail rotor is an 8 in. propeller (DJI-8045) driven by a 920 kV brushless outrunner motor (DJI 2212). For attitude stabilization of the vehicle, an onboard 3 g processor-sensor board was incorporated.

An efficient lightweight cyclorotor design is key to developing a flightworthy vehicle. The cyclorotor design was optimized for hover by using the understanding obtained from extensive experimental studies discussed in [9,10]. The goal of these studies was to maximize power loading and to obtain the required thrust at a low rotational speed to keep the centrifugal force within manageable levels. Based on these studies, the following parameters for the cyclorotor were chosen, which resulted in the best aerodynamic performance: 1) blade area/rotor area and blade chord/radius ratio of 0.35 and 0.625, respectively; 2) maximum blade pitch angle of 45 deg; and 3) a NACA 0015 airfoil section incorporated in the blade.

Reducing the centrifugal forces is important to ensure structural integrity of the cyclorotor. This is possible by implementing

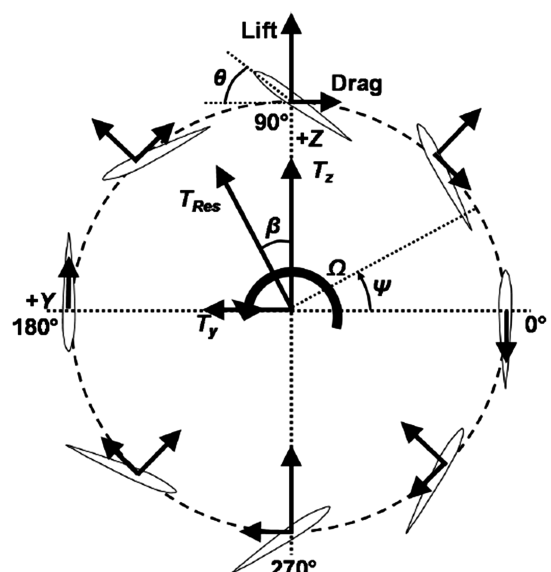


Fig. 6 Blade pitching kinematics and force vectors on a cyclorotor in hover condition.

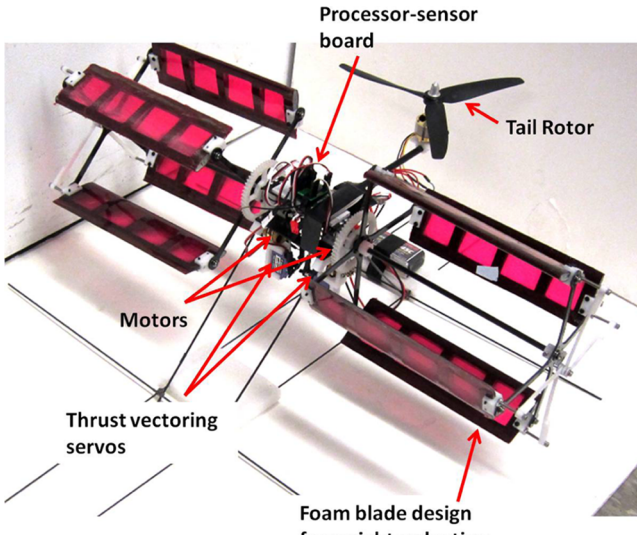


Fig. 7 Twin-rotor cyclocopter MAV.

lightweight and innovative designs for both the blade and the rotor supporting structure. Based on multiple iterations, the final blade design shown in Fig. 8 is chosen. It consists of a monolithic blade design with a single layer of carbon prepreg over a foam core with multiple rectangular sections removed. A 50- μm -thick mylar film is used to cover the blade surface. The final weight of a single blade was 6 g.

The rotor structure was optimally designed to withstand the centrifugal forces. As shown in Fig. 9, the key structural elements are the two end plates machined out of 0.0625-in.-thick carbon-fiber

laminate. The tip of each arm of the end plate houses a pitch bearing about which the blades can freely rotate. A hollow rotor shaft was cantilevered from the root end on two bearings. This shaft is nonrotating so that the blade pitch mechanism mounted at the tip of the shaft could be placed in the stationary frame. The motor only drives the root end plate, and the torque is transferred to the tip end plate through the blades. To pitch the blades in a cyclic manner, a passive pitch mechanism was incorporated using a four-bar linkage mechanism. The direction of the thrust vector is changed by varying the offset direction as shown in Fig. 10. To rotate the offset link, a servo with a total swivel angle of 60 deg is installed, which provides ± 30 deg of thrust vectoring capability.

The key design parameters and weight breakdown are given in Tables 1 and 2, respectively.

IV. Control Methodology

To conduct system-identification tests, it is important to ensure that the vehicle can be consistently flown in hover. From preliminary flight-test observations, it was seen that the vehicle is unstable in an open-loop condition. Hence, a feedback control system needs to be incorporated for achieving hover flight. This section describes the attitude control implementation and hover-flight testing of the twin cyclocopter.

A. Avionics and Telemetry

For vehicle state computation and control tasks, a lightweight (1.5 g) processor-sensor board (GINA2.2c, developed by the University of California, Berkeley [13]) is incorporated on the vehicle as shown in Fig. 11. The principal components of the board are a TI MSP430 microprocessor for onboard computation tasks, ITG3200 triaxial gyros, KXSD9 triaxial accelerometer, and a 2.4 GHz ATMEL transceiver for wireless communication tasks. To retrieve state and actuator input information in real time, bidirectional communication is implemented. The time-critical inner-loop feedback occurs at an update time period of 6 ms. To provide for trim adjustments and ground-station control, a 2.4 GHz ATMEL AVR transceiver communicates wirelessly with the onboard controller as shown in Fig. 12 using a LabVIEW interface.

B. Attitude Control

Pitch, roll, and yaw attitude control for the present vehicle is obtained through a combination of rotational speed control and thrust vectoring of the cyclorotors. As mentioned previously, the cyclorotors rotate in the same direction such that the blades on top are advancing in the forward direction. This creates a nose-up pitching moment, which is counterbalanced by a tail rotor thrusting upward. Therefore, pitch control is achieved by directly controlling the tail rotor thrust as shown in Fig. 13. For roll control, the rotational speeds of the two cyclorotors are varied in a differential manner as shown in Fig. 14. Finally, yaw control is achieved by tilting the thrust vectors in opposite directions as shown in Fig. 15. It should be noted that, in an unconstrained setup, the roll and yaw degrees of freedom are tightly coupled due to gyroscopic effects. This will be discussed in detail in Sec. V.

The gyros measure the pitch q , roll p , and yaw r attitude rates, while the accelerometers record the body-axis translational accelerations. The linear accelerations are neglected because hover is the flight condition of interest. As a result, the tilt of the gravity vector can be extracted from accelerometer measurements. Integrating gyroscope measurements leads to drift, while accelerometers are sensitive to vibrations. Therefore, a complementary filter was incorporated to extract the pitch and roll Euler angles using a high-pass filter for the gyros (4 Hz cutoff) and a low-pass filter for the accelerometers (6 Hz cutoff). The rotor vibrations were filtered out because these were sufficiently higher than those of the body dynamics.

Onboard inner-loop feedback was implemented using a proportional-derivative controller as shown in Fig. 16. The feedback states were the pitch and roll Euler angles (θ, ϕ) and body-axis angular rates (p, q , and r). An outer-loop feedback capability was

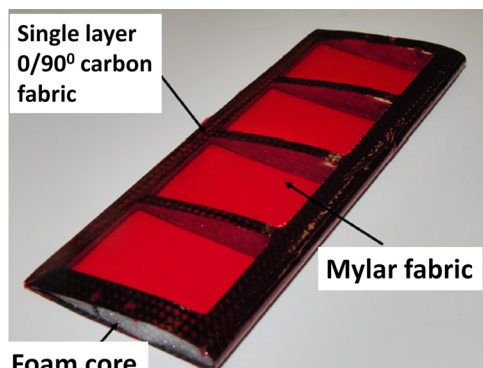


Fig. 8 Blade construction.

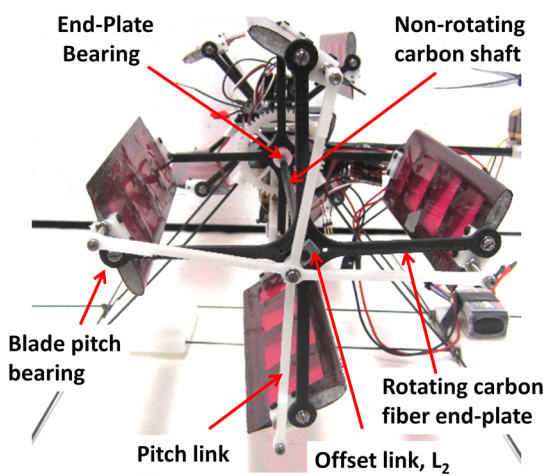


Fig. 9 Rotor structure and pitch link mechanism.

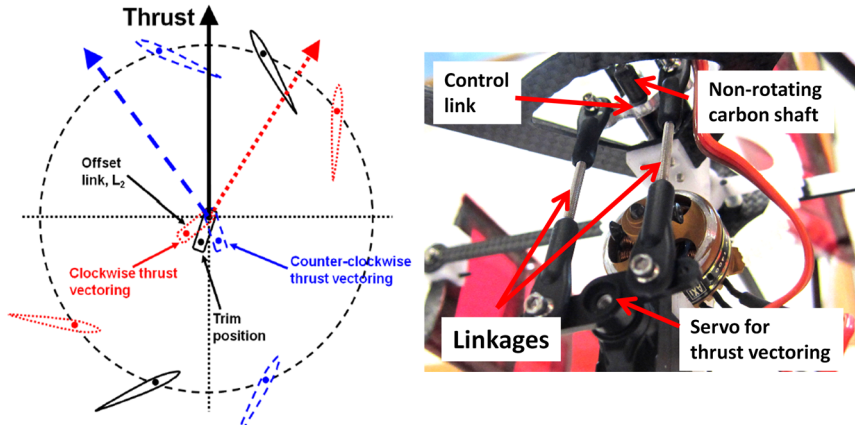


Fig. 10 Thrust vectoring on cyclorotor.

provided for translational positioning by a human pilot or a position-tracking system such as Vicon. The final control inputs to the vehicle actuators are the individual revolutions per minute for the two cyclorotors and tail rotor and the two servo inputs as shown in Fig. 16.

C. Hover-Flight Testing

Before free-flight testing, it was necessary to investigate the closed-loop attitude stability of the vehicle on a constrained setup. This was achieved by mounting the vehicle on a spherical gimbal, which restricted the vehicle in translation but allowed free rotation in pitch, roll, and yaw. A Ziegler–Nichols-based tuning approach was used to arrive at suitable feedback gains. It should be noted that achieving stable attitude in the gimbal setup was an important necessary condition to ensure stable free flight, and it also enabled quick troubleshooting with minimal damage to the vehicle. As mentioned earlier, the roll and yaw degrees of freedom were observed to be tightly coupled due to gyroscopic effects. Therefore, to decouple these responses, onboard control mixing is required. However this would corrupt the system-identification procedure due to correlation between the roll and yaw inputs. Hence, hover-flight testing was carried out without any mixing of the control inputs.

One important consideration is the fact that the cyclorotor is being driven through a plastic gearbox arrangement. The high vibratory

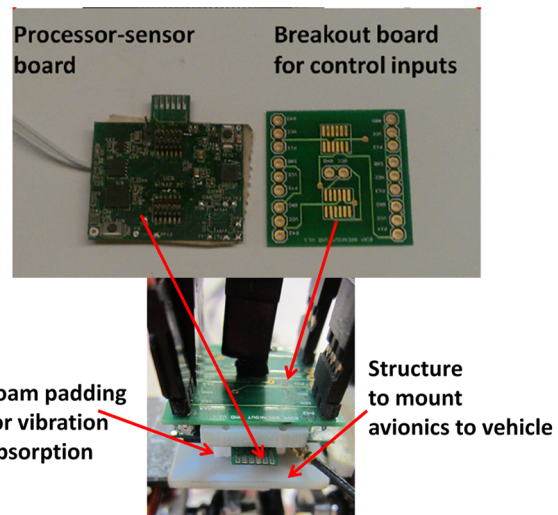


Fig. 11 Onboard processor-sensor board (GINA).

Table 1 Design Specifications for twin cyclocopter

Design feature	Twin cyclocopter
Cyclorotor diameter	6 in.
Blade span	6.25 in.
Blade chord	2 in.
Blade airfoil section	NACA 0015
Blade pitch amplitude	± 45 deg
Blade pitch axis	45% from LE
Cyclorotor motor	AXI 2204/54 outrunner
Cyclorotor gear ratio	7.5:1
Thrust vectoring servo	Blue Bird BMS-366X
Processor-sensor board	GINA 2.2c [13]
Battery	45 C three-cell 850 mA · h

Table 2 Weight breakdown of twin cyclocopter

Component	Weight, g
Cyclorotor (combined)	155
Pitch mechanism plus servos	31
Structure plus landing gear	75
Motors plus transmission	74
Li-po battery	75
Electronics plus wiring	20
Tail rotor	70
Total	500

environment coupled with changes in the cyclorotor torques can lead to significant oscillations along the pitch degree of freedom. Therefore, for stable flight, it is extremely important to ensure that the tail rotor responds quickly to these rapid changes in torque. The tail rotor brushless motor control is provided by a commercial off-the-shelf speed controller [Turnigy 12-A electronic speed controller (ESC)]. A typical ESC takes in pulse-width-modulated inputs (up to 1 kHz) from the onboard flight controller and converts them into high-frequency (greater than 8 kHz) three-phase voltage inputs to the brushless motor. The firmware on the ESC chip introduces a hysteresis in the three-phase signals so that the output to the motor is smooth. Although this is adequate for conventional rotor operations, it is not so for multicopter applications, and especially for the tail rotor in the cyclocopter. Therefore, modifications to the firmware are required to remove this hysteresis and ensure that there is rapid tail rotor rpm response to control inputs. These changes were seen to be critical for flight stability.

After accounting for the previous considerations, flight tests were performed to carefully determine trim values to ensure that the cyclorotor thrust vectors are in the vertical direction and to avoid other undesirable couplings in the pitch, roll, and yaw degrees of freedom. Following this, satisfactory hover flight was achieved, as shown in Figs. 17 and 18.

V. Flight Dynamics Identification

The relatively superior aerodynamic performance of the cyclocopter has been shown previously. However, it may also have



Base station transceiver **Onboard transceiver**

Fig. 12 Schematic showing the wireless telemetry.

potential for rejecting larger magnitudes of gust as well as for greater maneuverability. The previous flight tests were done with onboard proportional-derivative controllers. It is expected that the control methodology can be significantly improved with model-based, optimal, and robust controllers. To develop the maneuverability and disturbance characteristics of the bare airframe and to enable implementation of model-based controllers, there is a need to identify the six-degree-of-freedom (6-DOF) flight dynamics model of the cyclocopter. A description of the identification methodology and results is given in the following sections.

A. Methodology

To estimate the model parameters, systematic input-excitation experiments of the vehicle are conducted, and all the relevant states are measured. From knowledge of the inputs and outputs, system-identification techniques can be applied to determine the vehicle dynamics. The experimental setup of the vehicle in a typical input-excitation flight test is shown in Fig. 19. A series of infrared cameras (Vicon) measure the movement of retroreflective markers placed on the vehicle. From these, the translational and rotational states of the vehicle are measured at a frequency of 167 Hz. The onboard flight controller relays inputs from the ground station and transfers it to the onboard actuators. A latency of about 30 ms between the input and corresponding output was present due to wireless communication delay, onboard loop rate, and actuator lag. The translational states measured by Vicon and the rotational states and actuator inputs measured by the onboard microcontroller were synchronized with a common timestamp in the ground station.

For input-excitation experiments, a series of lateral, longitudinal, yaw, and heave inputs were given in separate independent flight tests. The input frequencies were varied up to about 20 rad/s for the lateral, longitudinal, and yaw states. The input frequencies for the heave states were lower due to the inherently slower dynamics. A total of 25 flight tests were conducted to extract the model parameters with error estimates. The inputs were provided by a pilot rather than a chirp input program for two reasons: 1) pilot inputs have better spectral richness [14], and 2) it was difficult to keep the body in trim with computerized inputs.

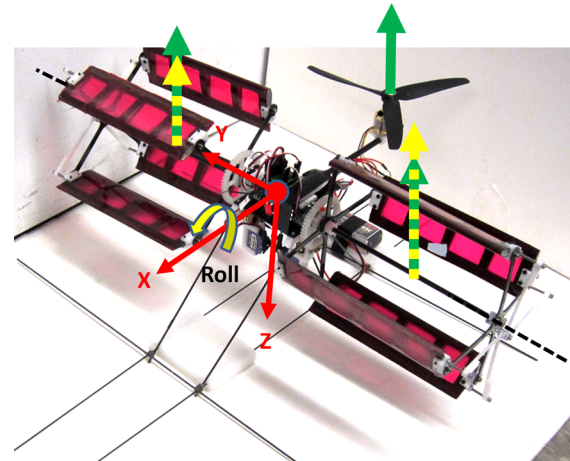


Fig. 14 Roll control with trim values (solid) and control input (dashed).

1. Bare Airframe Dynamics with Feedback Regulation

It is generally desirable to conduct input-excitation flight tests in an open-loop condition while ensuring that the vehicle can be kept in trim before and after input excitation. However, highly maneuverable and unconventional small-scale fliers being explored recently are generally unstable due to either the lack of, or insufficient, aerodynamic damping in the system. This is definitely the case for the cyclocopter, considered in this study. Therefore, the vehicle can quickly go out of trim even after benign inputs. To conduct flight tests in a safe manner, it is essential to implement feedback regulation for stability in hover. For the present flight tests, a proportional derivative controller with respect to its attitude states was used.

Figure 20 shows a schematic of the information flow with feedback control active. Conventional treatment regards δ_{pilot} as the input. However, this would imply an identification of the closed-loop vehicle dynamics. The primary interest is a knowledge of the bare airframe dynamics. Therefore, the inputs directly fed into the actuators (δ_a) are considered. This would then enable the extraction of the bare airframe dynamics from closed-loop data.

However, there are some issues with closed-loop system identification. These are as follows.

- 1) Low-frequency pilot inputs are suppressed.
- 2) Correlation between the control inputs can be induced.
- 3) Correlation between actuator inputs and states due to external disturbances such as turbulence can also occur.

The problem of low signal-to-noise content in low-frequency data can be reduced by decreasing the feedback gains to a value sufficient for safe flight testing. However, this is still an inherent problem with identification of unstable systems and is a common occurrence. Now, the correlation between control inputs can be an issue for the cyclocopter because a coupling between the roll and yaw degrees of

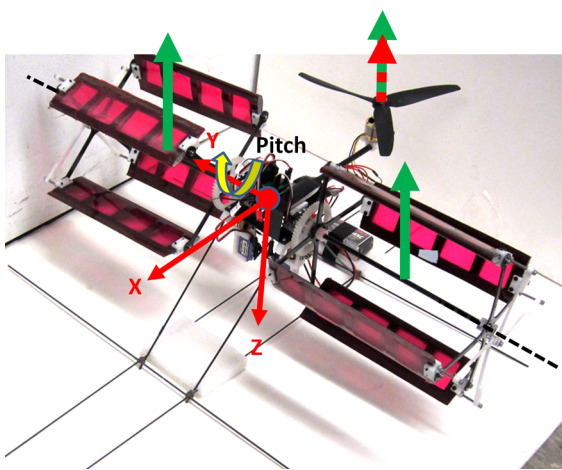


Fig. 13 Pitch control with trim values (solid) and control input (dashed).

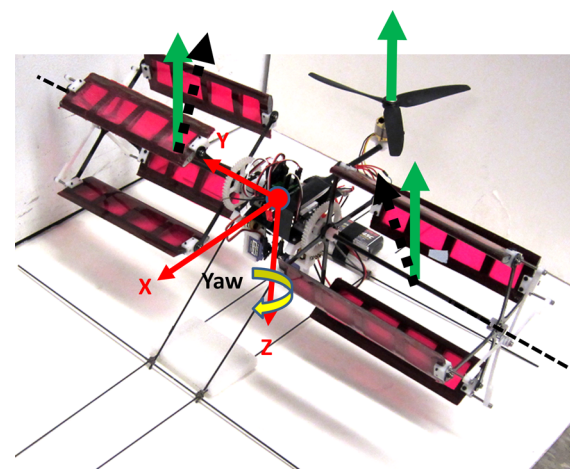


Fig. 15 Yaw control with trim values (solid) and control input (dashed).

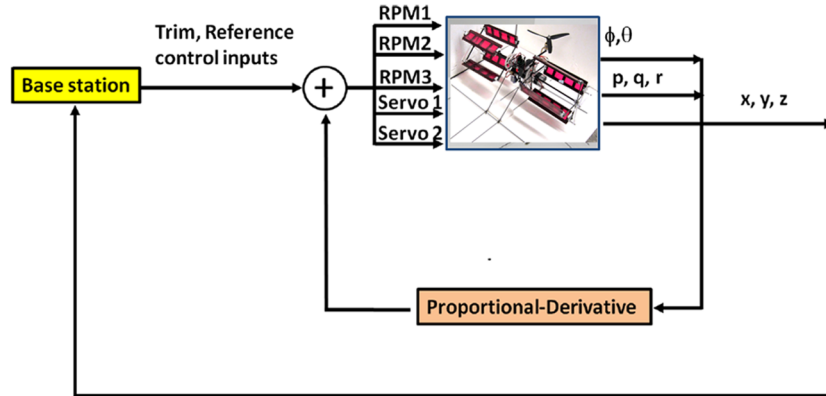


Fig. 16 Feedback control.

freedom was observed in flight tests. However, this problem can be addressed as follows. Let the primary response considered in a particular flight be roll. The pilot provides pure lateral inputs in the open-loop condition. The secondary yaw response would actuate the yaw inputs due to feedback. However, these secondary inputs are completely correlated with the yaw response and therefore are

implicitly included in the identification process through the yaw-rate response. Hence, if care is taken to provide only primary inputs, with secondary inputs kept to a minimum in the open-loop condition, the problem of control input correlation can be alleviated. Finally, the issue of actuator input correlation with external noise is not of primary concern in the present case because the flight tests were performed in an indoor environment with quiescent air conditions. The only source of correlation is the measurement noise, which is primarily from the rotor vibrations. Because these frequencies were significantly higher than the body dynamic frequencies of interest, they were filtered using zero phase lag filters during postprocessing (using a fourth-order low-pass Butterworth filter with 15 Hz cutoff).

The minimum attitude rate feedback gains used for the system-identification flight tests that resulted in acceptable hover performance were 200, 84, and 160 $\mu\text{s}/\text{rad}$ for the pitch, roll, and



Fig. 17 Hover flight of twin cyclocopter.

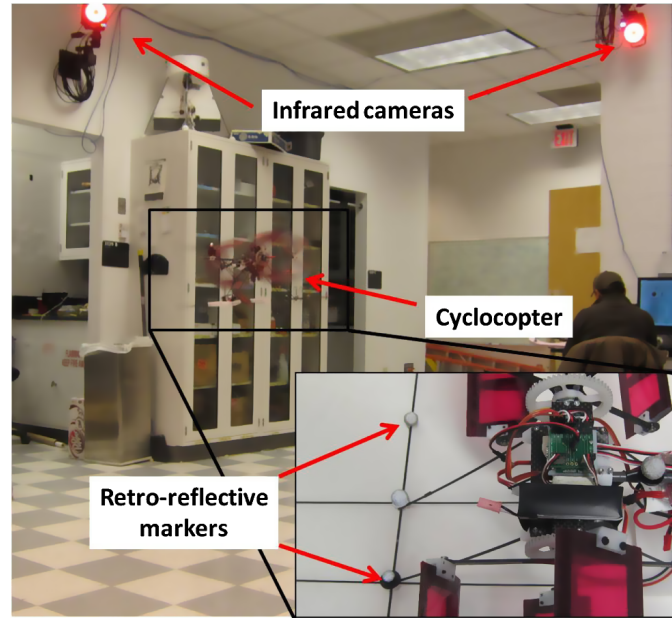
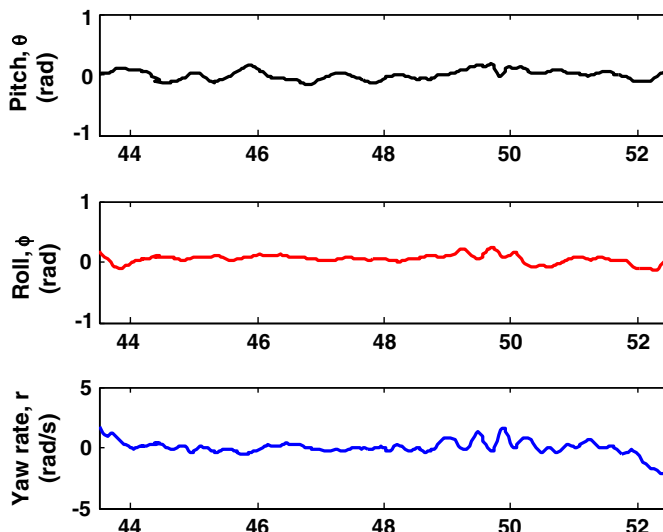
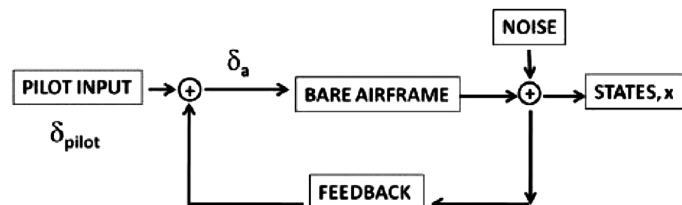


Fig. 19 Flight-test setup.



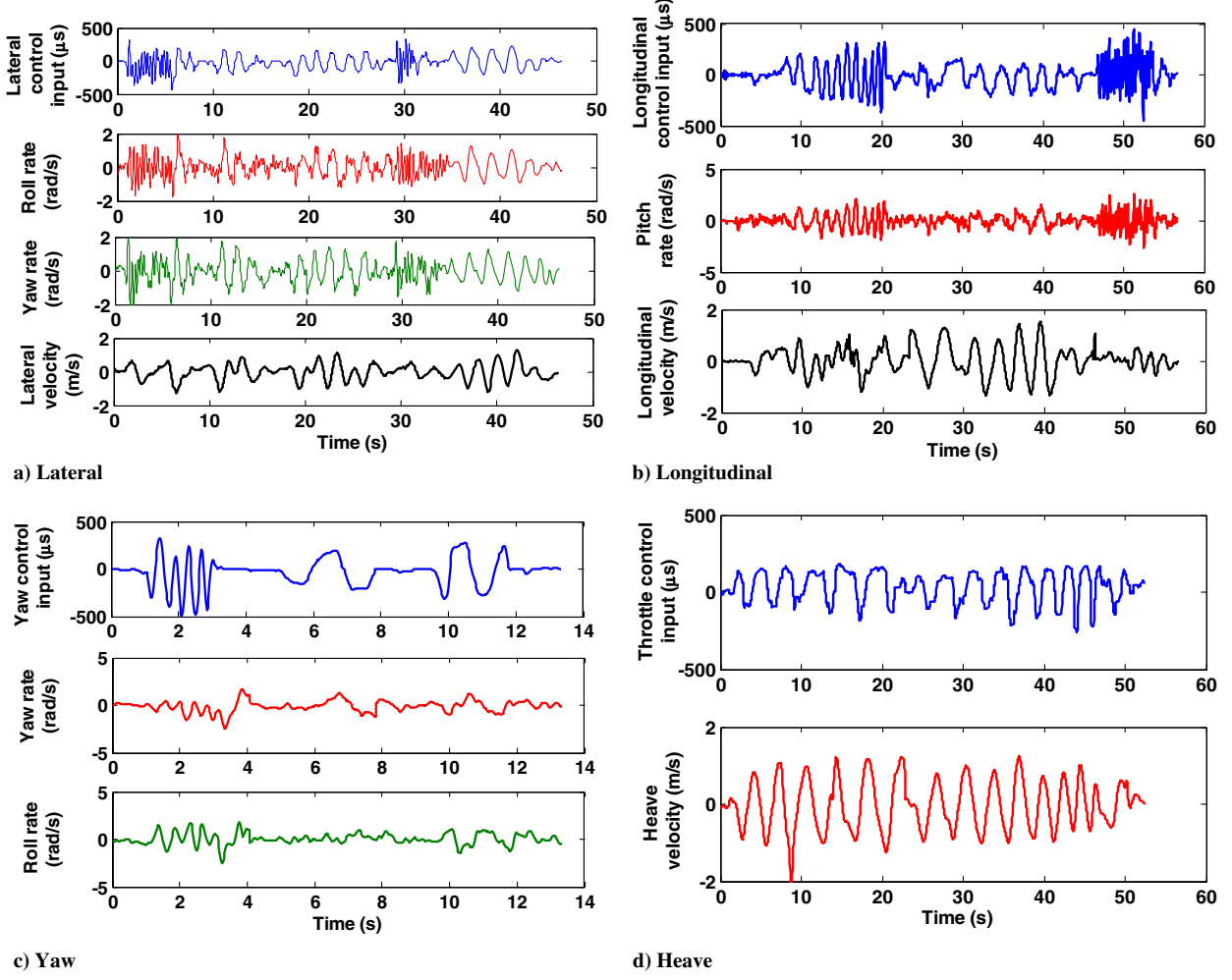


Fig. 21 Sample time-history data from input-output flight tests of cyclocopter in hover.

yaw degrees of freedom. It must be mentioned that, because of the unstable nature of the vehicle, limited flight space with respect to vehicle size, and absence of control cross-coupling that might have otherwise aided flight stability, good spectral information in the input-output data was not obtained. As a result, time-domain methods were employed (SIDPAC [15]) as opposed to frequency-

domain methods. Because the dynamics were expected to be unstable, equation-error methods were used [16].

2. Model Structure

A basic model structure of the vehicle needs to be formulated to draw meaningful relations between the inputs and the outputs. A linear time-invariant reduced-order model is considered in this paper. The model can be represented in state-space form as

$$\dot{\mathbf{x}} = \mathbf{Ax} + \mathbf{Bu} \quad (1)$$

where $\mathbf{x} = [u \ v \ w \ p \ q \ r \ \phi \ \theta \ \psi]$ is the state vector, $\mathbf{u} = [\delta_{\text{lat}} \ \delta_{\text{lon}} \ \delta_{\text{throttle}} \ \delta_{\text{rudder}}]$ is the control input vector, and \mathbf{A} and \mathbf{B} are the stability and control derivative matrices, respectively. The longitudinal, lateral, and heave velocity states are given by u , v , and w respectively. The pitch, roll, and yaw attitude rate states are p , q , and r , respectively. The Euler angles are ϕ (roll), θ (pitch), and ψ (yaw). The longitudinal control input δ_{lon} is the tail rotor power. Differential revolutions per minute input to the two cyclorotors constitutes δ_{lat} , and the yaw input is the differential motion of the thrust vectoring servos. Throttle is provided by simultaneously increasing the revolutions per minute of the cyclorotors as well as of the tail rotor. To further simplify the model structure, it is assumed that the longitudinal and heave degrees of freedom are independent and decoupled from the rest of the dynamics. Based on these, the model structure is shown in Eq. (2). It is noted that the model structure shown is identified using statistical model structure determination methods described later:

Parameter	Value	Standard error	F_P (minimum 20)
Longitudinal mode			
X_u , 1/s	-1.1	0.061	710
M_u , rad/m/s	4.7	0.38	120
M_q , 1/s	0.6	0.2	25
M_{lon} , rad/s ²	-47	4.35	410
Lateral and yaw mode			
Y_v , 1/s	-0.55	0.15	680
L_v , rad/m/s	-2.1	0.3	90
L_p , 1/s	0.2	0.1	23
L_r , 1/s	-9.2	0.46	310
L_{lat} , rad/s ²	33	3.81	650
L_{rud} , rad/s ²	-24	2.81	120
N_v , rad/m/s	-2.4	0.57	35
N_p , 1/s	6.6	0.59	370
N_r , 1/s	0.1	0.1	24
N_{lat} , rad/s ²	41	3.56	95
N_{rud} , rad/s ²	18.7	1.55	162
Heave			
Z_w , 1/s	-0.55	0.037	810
Z_{thr} , m/s ²	-15	0.8	650

$$\begin{aligned}
 \begin{pmatrix} \dot{u} \\ \dot{v} \\ \dot{w} \\ \dot{p} \\ \dot{q} \\ \dot{r} \\ \dot{\phi} \\ \dot{\theta} \end{pmatrix} &= \begin{bmatrix} X_u & 0 & 0 & 0 & 0 & 0 & 0 & -g \\ 0 & Y_v & 0 & Y_p & 0 & Y_r & g & 0 \\ 0 & 0 & Z_w & 0 & 0 & 0 & 0 & 0 \\ 0 & L_v & 0 & L_p & 0 & L_r & 0 & 0 \\ M_u & 0 & 0 & 0 & M_q & 0 & 0 & 0 \\ 0 & N_v & 0 & N_p & 0 & N_r & 0 & 0 \\ 0 & 0 & 0 & 1 & 0 & 0 & 0 & 0 \\ 0 & 0 & 0 & 0 & 0 & 1 & 0 & 0 \end{bmatrix} \begin{pmatrix} u \\ v \\ w \\ p \\ q \\ r \\ \phi \\ \theta \end{pmatrix} \\
 + & \begin{bmatrix} 0 & 0 & 0 & 0 \\ 0 & 0 & 0 & 0 \\ 0 & 0 & Z_{\text{thr}} & 0 \\ L_{\text{lat}} & 0 & 0 & L_{\text{rud}} \\ 0 & M_{\text{lon}} & 0 & 0 \\ N_{\text{lat}} & 0 & 0 & N_{\text{rud}} \\ 0 & 0 & 0 & 0 \\ 0 & 0 & 0 & 0 \end{bmatrix} \begin{pmatrix} \delta_{\text{lat}} \\ \delta_{\text{lon}} \\ \delta_{\text{throttle}} \\ \delta_{\text{yaw}} \end{pmatrix} \quad (2)
 \end{aligned}$$

B. Results and Discussion

1. Time-History Data

Segments of the input–output time-history data for the lateral, longitudinal, yaw, and heave directions are shown in Fig. 21. The units for the control inputs are in microseconds, which corresponds to the pulse-width-modulated signal sent to the actuators. The maximum value is 1000. For the identification, the inputs are scaled by the maximum value such that $u_{\text{input}} \in [-1, 1]$. By keeping consistent input limits, the control derivatives can be compared across various vehicle platforms regardless of the type of actuator.

For the flight tests, it was observed that the off-axis responses for the longitudinal and heave degrees of freedom were negligible. Therefore, the assumption that they are independent and decoupled is valid. However, from Figs. 21a and 21c, it can be clearly seen that there is significant coupling between the roll and yaw degrees of freedom for both lateral and rudder (yaw) being the primary control inputs. Therefore, the inclusion of the stability and control derivatives such as L_r , N_p , N_v , L_{rud} , and N_{lat} is required. The effect of feedback regulation on suppressing attitude rate information for low-frequency inputs is clear from Fig. 21b. Additionally, it can be seen that the translational velocity states are bandwidth-limited for high-frequency inputs (Fig. 21b). These effects were taken into account in the time-domain identification process.

2. Model Identification

The stability and control derivatives were extracted from the time-history data using equation-error methods. To determine the statistical significance, or linear relationship, between the measured dependent variable and a set of regressor vectors, the partial F-ratio F_p is used to test the contribution of an individual parameter (such as L_p) to the overall identification estimate. Any regressor with F_p less than a cutoff value is removed from the model. For 95% confidence, the cutoff value is taken as 20 [15]. The results of the identified parameters for the various dynamic modes are given in Table 3. Although unmodeled nonlinear effects and presence of feedback regulation may reduce accuracy, the R^2 values for all the identified modes were between 75 and 88%, indicating acceptable identification accuracy. The parameter values were corrected for colored residuals, and the standard error was found to be within 10%.

To verify the identified model, it is important to compare the output of the model to a set of input–output data different from what was used to estimate the parameters. A few time-domain verification plots

in the translational velocity, attitude velocity, heave, and yaw modes are shown in Fig. 22. It is noted that, for the verification, a data set different from the ones used for model identification was used. Additionally, the comparison between angular rate derivatives as opposed to angular rates is shown because equation-error methods are employed. It can be clearly seen that all the modes have satisfactory comparison between flight data and the predicted output from the model. There is an overall agreement between the flight data and model output, which suggests that the proposed reduced-order model is acceptable. The R^2 values for the model verification were between 75–90% for the cases considered and are comparable to the values obtained during model identification.

Longitudinal mode: The identified stability and control derivatives for the longitudinal mode are shown in Table 3. It can be seen from the sign of the longitudinal translation derivative X_u that it is stabilizing. If a velocity perturbation in the X direction is given, then a stabilizing force is generated in the direction that tends to reduce this perturbation. From the value of M_u , a nose-up pitching moment is produced as the vehicle moves forward. These are visualized in Fig. 23. Although the stabilizing nature of these forces is desired, the magnitude of the parameters X_u and M_u will have an impact on the gust disturbance rejection as well as forward flight capability, which will be discussed later. It can also be observed from M_q that the pitch damping is unstable. This explains the requirement of feedback damping to stabilize the vehicle in pitch. It must be noted that no significant coupling between pitch and heave was observed (the M_w and Z_q terms were not significant).

Lateral and yaw mode: From Table 3, it can be seen that, similar to X_u , the lateral translation derivative Y_v is stabilizing. However, the magnitude of Y_v is about one-half that of X_u . This is probably because of a lower body area when the vehicle faces a lateral perturbation as opposed to a longitudinal perturbation. Additionally, the aerodynamic damping provided by the rotors to a longitudinal velocity perturbation can possibly be higher because it directly influences the effective angle of attack of the blades when they reach the front portion of the circular trajectory. The force and moment response for a given lateral perturbation is shown in Fig. 24. When the vehicle moves right, or if there is a v perturbation along the Y axis, in addition to a roll-left moment L_v , there is a counterclockwise yaw moment N_v . This is possibly because the net drag due to a v perturbation is offset from the c.g. location, which induces a yaw moment. Similar to M_q , the roll and yaw attitude rate stability derivatives L_p and N_r are marginally unstable as well.

However, the most important characteristic of the vehicle is the strong gyroscopic coupling between the roll and yaw stability and control derivatives L_r , L_{rud} , N_p , and N_{lat} . This is explained in Fig. 25. When a roll-right control moment is given, a roll-right as well as a clockwise motion follows. Similarly, when a clockwise control moment is given, a clockwise as well as a roll-left response occurs. This is because both the rotors are spinning in the same direction such that the net angular momentum is along the $-Y$ axis. Any disturbance to this angular momentum results in a gyroscopic-coupled response. This is a unique property of the twin cyclocopter and has to be accounted for in the control system to achieve decoupled response.

Heave mode: The heave mode is an independent and decoupled degree of freedom and is damped, as can be observed from Z_w . It might be expected that the magnitude of Z_w and X_u should be similar because the cyclorotor frontal area facing the respective perturbations is similar. However, a careful observation of Fig. 26 shows that the blade attains different pitch angles at different positions of its trajectory. It is around 40–45 deg at the top and bottom, which can be expected to be close to stall. Now, a heave perturbation mainly affects the blades in the top and bottom positions. The corresponding restoring force at such high blade pitch angles are expected to be lower than when a longitudinal perturbation is given, which affects the blades in the front and back with a lower blade pitch angle. This may explain the relatively higher magnitude of X_u .

Eigenstates: Based on the identified stability derivatives from Table 3, the eigenvalues can be computed. These are shown in Table 4 and Fig. 27. As observed before, the longitudinal rotation rate is

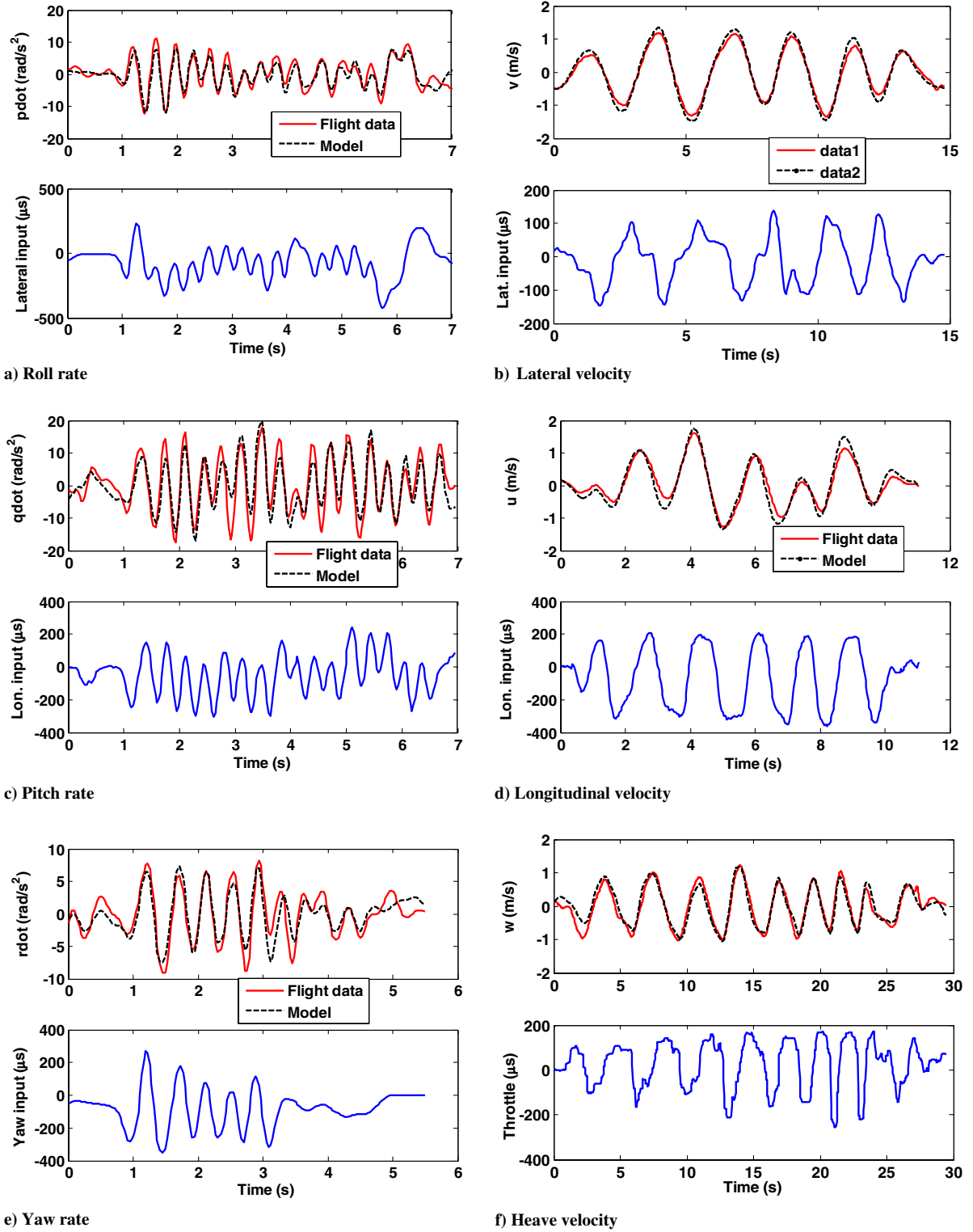


Fig. 22 Verification between flight data and model estimate using the identified parameters.

oscillatory and unstable, whereas the translation mode is damped and nonoscillatory. The heave mode is also damped. The influence of the gyroscopic coupling can be seen in the lateral-yaw rotation eigenvalues, which are marginally unstable and highly oscillatory. Two other eigenvalues indicate that the coupling between the lateral translation and directional modes is present, with one of them being stable and the other unstable. It can be seen that the open-loop flight dynamics of the cyclocopter is highly coupled in the lateral and directional modes. Therefore, there is potential scope to improve flight performance by implementing model-based optimal linear quadratic regulation control and robust H_∞ control in the future.

VI. Maneuverability and Disturbance Rejection Analysis

Based on the identified model described previously, it is of interest to characterize the maneuverability and gust disturbance rejection potential of the vehicle that is independent of any control methodology implemented on this system. Hence, a systematic framework of metrics can be established that can help compare the cyclocopter system with various other MAV systems such as shrouded rotors, flybarless helicopters, and microquadrotors. This section describes the development of these metrics for the cyclocopter.

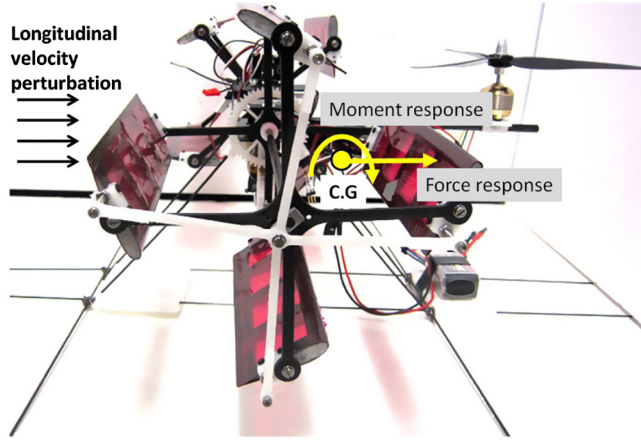


Fig. 23 Response to a perturbation in longitudinal translation.

A. Maneuverability Analysis

The controllability Gramian is a measure that is typically used to determine if a given system is controllable or not. However, certain properties of the Gramian can be used to provide more useful insights on the vehicle characteristics. Consider the state-space representation of the linear time-invariant system $\dot{x} = Ax + Bu$. The state x is said to be controllable if, given an initial state x_0 at $t = 0$, there exists an input $u(t)$ for $0 \leq t \leq t_f$ that yields a final state x_f at $t = t_f$.

A controllability operator $\Psi_c: u \rightarrow x(\tau)$, which maps an input $u(t)$ to a final state $x(t_f)$, can be expressed as

$$x(0) = x_f = \Psi_c u = \int_{-\infty}^0 e^{-At} Bu(t) dt \quad (3)$$

The system is controllable if all the states of the system can be brought to arbitrary values through suitable inputs. To verify controllability, the controllability Gramian of the matrix pair (A, B) defined in Eq. (4) has to be nonsingular [17]:

$$X_C = \Psi_c \Psi_c^* = \int_{-\infty}^0 e^{-At} BB^* e^{-A^*t} dt \quad (4)$$

If the system is controllable, a key question arises. What are all the final states given by Eq. (3) that can result from an input u of unit norm? From [17], it can be shown that, if we define

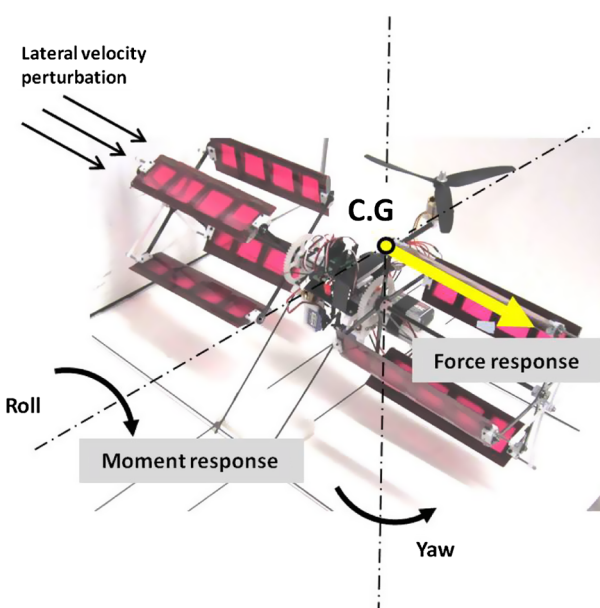


Fig. 24 Response to a perturbation in lateral translation.

$$x_C = X_C^{-1/2} \Psi_c u \quad (5)$$

then the final states reachable are given by

$$x_f = X_C^{-1/2} x_C \quad (6)$$

with $|x_C|^2 \leq \|u\|_2^2 \leq 1$. The boundary of all reachable states given by Eq. (3) can be defined by the controllability ellipsoid:

$$\epsilon_C = \{X_C^{-1/2} x_C: |x_C| = 1\} \quad (7)$$

It is easy to see that, if the ellipsoid is bigger, the reachable states are larger for a given input. This implies that the system has more maneuverability, which is a very useful practical consequence of determining the size of the ellipsoid. The other key information is to determine which states are more sensitive to a given input. This can be obtained from the eigenvectors and eigenvalues of the controllability ellipsoid.

Let v_1, v_2, \dots, v_n be the eigenvectors of the ellipsoid for an n -state system and $\mu_1, \mu_2, \dots, \mu_n$ be the corresponding eigenvalues. For a controllable system, it can be shown that the eigenvalues of X_C are positive, and the final value of each state can be represented as

$$x_{0_i} = \mu_i v_i \quad (8)$$

which forms the principal axes of the ellipsoid. Consider two directions v_k and v_l , shown in Fig. 28. If $\mu_k > \mu_l$, then the state $x_k = \mu_k v_k$ is said to be more controllable than x_l , or in other words, it is more sensitive to a given input.

Now, it is likely that different vehicle systems would have different controllability ellipsoids or reachable spaces. Therefore, it is useful to compare the controllability of these vehicles by observing the properties of their respective ellipsoids. Two such ranking criteria can be extracted for a unit norm input: the Frobenius norm and the volume.

The Frobenius norm is

$$\|X_C^{1/2}\|_F = \sqrt{\{\text{trace}[(X_C^{1/2}, X_C^{1/2})]\}} \quad (9)$$

which is the square root of the sum of squares of the principal axis lengths of the controllability ellipsoid.

The volume is

$$\text{vol} = \det(X_C^{1/2}) \quad (10)$$

which is the volume of the reachable space or controllability ellipsoid.

To do this, the key is to determine the controllability Gramian X_C of the system using the continuous-time Lyapunov equation,

$$AX_C + X_C A^* + BB^* = 0 \quad (11)$$

It should be noted that the previous method works for a stable A matrix. However, we have determined that the cyclocopter is open-loop unstable. Therefore, special modifications are required.

The matrix A for the cyclocopter consists of stable and unstable eigenvalues. A transformation matrix is applied to decompose the matrix A into a stable (A_1) and an antistable (A_2) part, as shown in Eq. (12):

$$A \rightarrow \tilde{A} = TAT^{-1} = \begin{bmatrix} A_1 & 0 \\ 0 & A_2 \end{bmatrix} \quad B \rightarrow \tilde{B} = TB = \begin{bmatrix} B_1 \\ B_2 \end{bmatrix} \quad (12)$$

To compute the transformation matrix T , the eigenvalue decomposition of A is performed, $Au_i = \lambda u_i$, and the eigenvectors are split corresponding to the stable (S) and unstable (U) parts. The transformation matrix is then computed as shown in Eq. (13):

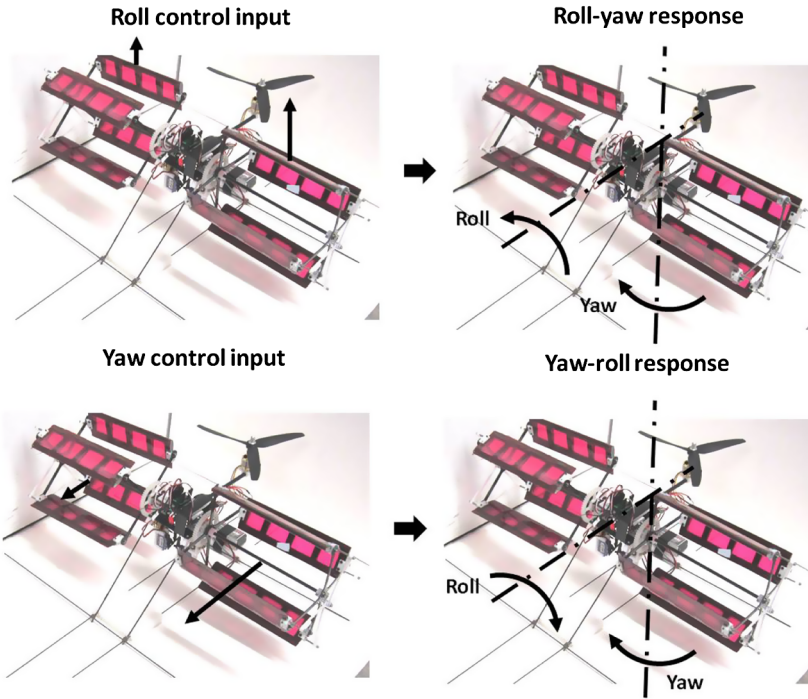


Fig. 25 Gyroscopic cross-coupling between roll and yaw degrees of freedom.

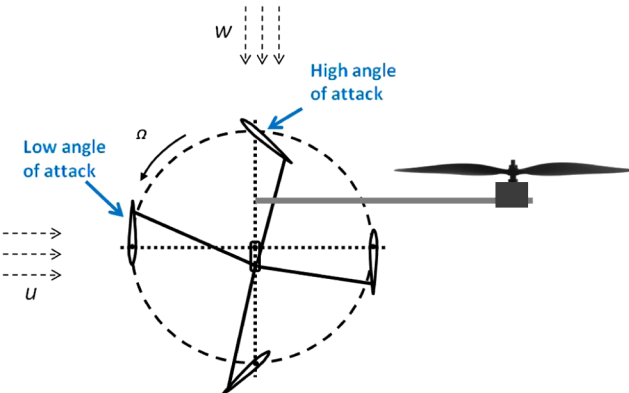


Fig. 26 Various blade pitch settings of cyclorotor.

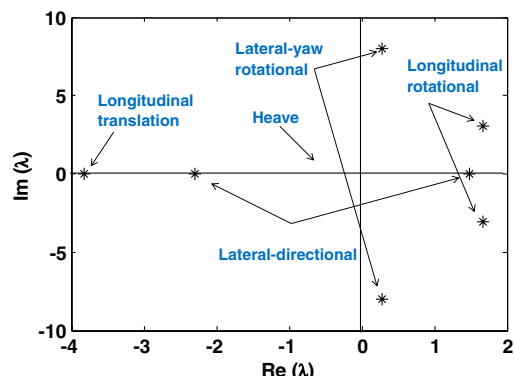


Fig. 27 Cyclocopter in hover: eigenvalues.

$$U_S = (u_1 \dots u_k), \quad U_U = (u_{k+1} \dots u_n) \quad T = (U_S U_U) \quad (13)$$

Let $P_1 \geq 0$, $P_2 \geq 0$ be the solutions of the following infinite-time Lyapunov equations:

$$A_1 P_1 + P_1 A_1^T + B_1 B_1^T = 0 \quad (-A_1) P_2 + P_2 (-A_2^T) + B_2 B_2^T = 0 \quad (14)$$

The solutions to Eq. (14) can be computed individually, and it can be shown [18] that the transformed controllability Gramian of the system is given by

$$X_C = T^{-1} \begin{bmatrix} P_1 & 0 \\ 0 & P_2 \end{bmatrix} (T^{-1})^T \quad (15)$$

Table 4 Cyclocopter in hover: eigenvalues

Mode	Eigenvalues	Damping	ω_n , rad/s
Longitudinal translation	-3.83		
Longitudinal rotation	$1.66 \pm 3.05i$	-0.48	3.47
Lateral directional	-2.29, 1.48		
Lateral-yaw rotation	$0.28 \pm 8.02i$	-0.035	8.02
Heave	-0.55		

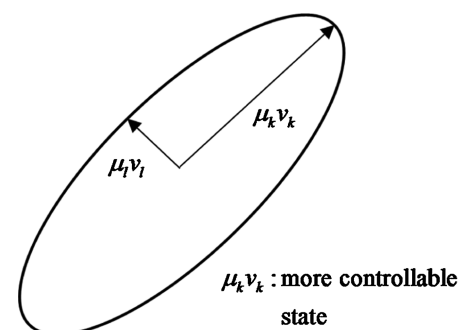


Fig. 28 Principal axes of controllability ellipsoid.

Once the controllability Gramian is computed, the controllability ellipsoid can be calculated, and the ranking criteria follow from the ellipsoid properties. Hence, the controllability of the unstable system can be determined.

As can be seen from Table 3, the longitudinal and heave modes are decoupled, whereas the lateral and yaw modes are coupled. For the present analysis, the longitudinal, lateral, and yaw dynamics will be considered. The A and B matrices are split accordingly as

Table 5 Controllability metric for cyclocopter

Mode	Frobenius norm
Longitudinal	18.9
Lateral yaw	79.6
Lateral yaw (without gyroscopic coupling)	47.6

$$A_{\text{LON}} = \begin{bmatrix} X_u & 0 & -g \\ M_u & M_q & 0 \\ 0 & 1 & 0 \end{bmatrix}, \quad B_{\text{LON}} = \begin{bmatrix} 0 \\ M_{\text{lon}} \\ 0 \end{bmatrix} \quad (16)$$

$$A_{\text{LAT-YAW}} = \begin{bmatrix} Y_v & 0 & 0 & g \\ L_v & L_p & L_r & 0 \\ N_v & N_p & N_r & 0 \\ 0 & 1 & 0 & 0 \end{bmatrix}, \quad B_{\text{LAT-YAW}} = \begin{bmatrix} 0 & 0 \\ L_{\text{lat}} & L_{\text{rud}} \\ N_{\text{lat}} & N_{\text{rud}} \\ 0 & 0 \end{bmatrix} \quad (17)$$

The states are $[uq\theta]$ and $[vpr\phi]$ for the longitudinal and lateral-yaw modes, respectively. Table 5 shows the controllability metrics calculated from Eq. (9).

The presence of the gyroscopic coupling control derivatives L_{rud} and N_{lat} result in a large value of the Frobenius norm for the lateral-yaw mode, as can be seen from Table 5. This implies that, for a given roll or yaw control input, the reachable states in the lateral or yaw direction are higher when the gyroscopic coupling terms are taken into account. This is important because it increases the overall maneuverability of the vehicle.

The overall controllability frobenius norm can be expressed as

$$\|X_C^{1/2}\|_F = \sqrt{\|X_C^{1/2}\|_{F_{\text{LAT-YAW}}}^2 + \|X_C^{1/2}\|_{F_{\text{LON}}}^2} = 81.8 \quad (18)$$

B. Disturbance Rejection Analysis

For the maneuverability analysis, the reachable space attained by the vehicle was calculated for a given control input. However, it is also of interest to observe which states are most sensitive to a given disturbance such as gusts. In the presence of aerodynamic disturbances such as gusts, the system dynamics can be expressed as

$$\dot{x} = Ax + D\xi \quad (19)$$

If $\xi = [\xi_u \xi_v \xi_p \xi_q \xi_r]$ represent the translational (u, v) and rotational (p, q, r) gust disturbances, respectively, then the disturbance matrix D consists of the negative of those stability derivatives that are affected by aerodynamic forces alone [19]. Hence,

$$D = -A_{\text{aero}} \quad (20)$$

Therefore, analogous to Eq. (1), the control input vector is ξ , and the control derivative matrix is D . Then, the infinite-time disturbance Gramian for a stable system is given by

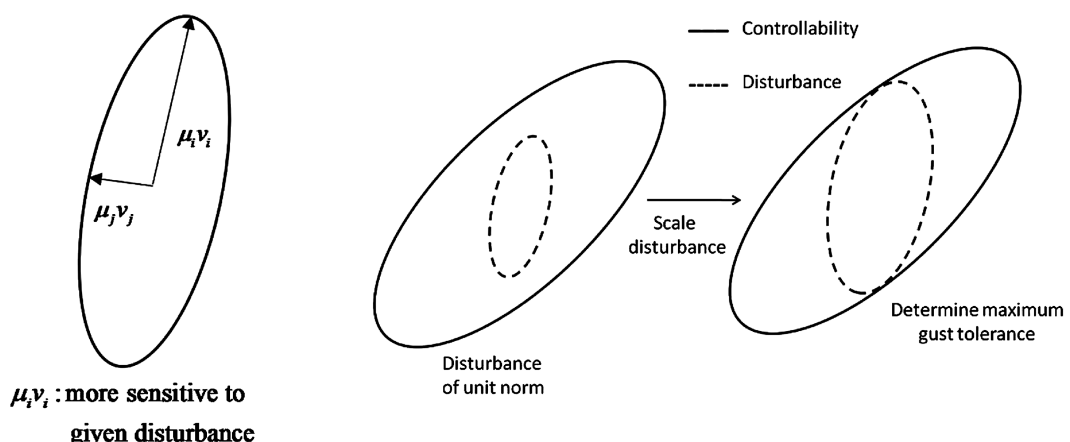


Fig. 29 Disturbance ellipsoid superimposed on the controllability ellipsoid.

$$X_D = \Psi_D \Psi_D^* = \int_{-\infty}^0 e^{-At} DD^* e^{-A^*t} dt \quad (21)$$

where X_D is the solution of the Lyapunov equation:

$$AX_D + X_D A^* + DD^* = 0 \quad (22)$$

If we define

$$x_D = X_D^{-1/2} \Psi_D \xi, \quad \|\xi\|_2^2 \leq 1 \quad (23)$$

then the disturbance ellipsoid can be expressed as

$$e_D = \{X_D^{1/2} x_D: |x_D| = 1\} \quad (24)$$

For a vehicle with unstable eigenvalues, the procedure similar to the controllability Gramian computation for unstable systems is adopted. Figure 29 shows the schematic of the disturbance ellipsoid along with a couple of its eigenstates. By inspection, we can say that the state $\mu_i v_i$ is more sensitive to a bounded disturbance than $\mu_j v_j$. Also, ranking criteria similar to the controllability ellipsoid can be drawn. We can also superimpose the controllability and disturbance ellipsoids for a given vehicle. As long as the disturbance ellipsoid is contained within the controllability ellipsoid, the vehicle can reject disturbances of unit norm. In other words, it would have the control power to overcome the disturbance. By scaling the disturbance vector until the disturbance ellipsoid reaches the limit of the controllability ellipsoid, the maximum gust amplitudes tolerated by the vehicle can be determined. It can be seen that the size and direction of the principal axes of the disturbance ellipsoid determine the extent of the gust rejection capability of the vehicle.

The maneuverability potential of the vehicle was characterized previously. We would also like to quantify the disturbance rejection tolerance of the vehicle when subjected to translational and rotational gusts. The aerodynamic-based stability derivatives influence the response of the vehicle to gusts. The longitudinal and lateral-yaw disturbance matrices are given next:

$$D_{\text{LON}} = \begin{bmatrix} -X_u & 0 \\ -M_u & -M_q \end{bmatrix}, \quad D_{\text{LAT-YAW}} = \begin{bmatrix} -Y_v & 0 & 0 \\ -L_v & -L_p & 0 \\ -N_v & 0 & -N_r \end{bmatrix} \quad (25)$$

It is noted that the stability derivatives L_r and N_p are considered to be dominated by gyroscopic effects and hence are not included in the disturbance matrices. The controllability and disturbance ellipsoids can then be superimposed to extract the gust-tolerance limits of the vehicle. Figure 30 shows a comparison between the two ellipsoids for the cyclocopter for a translational gust disturbance denoted by u_{gust} . The maximum states reachable by the vehicle are represented by the ellipsoid when subjected to a longitudinal control input of unit norm.

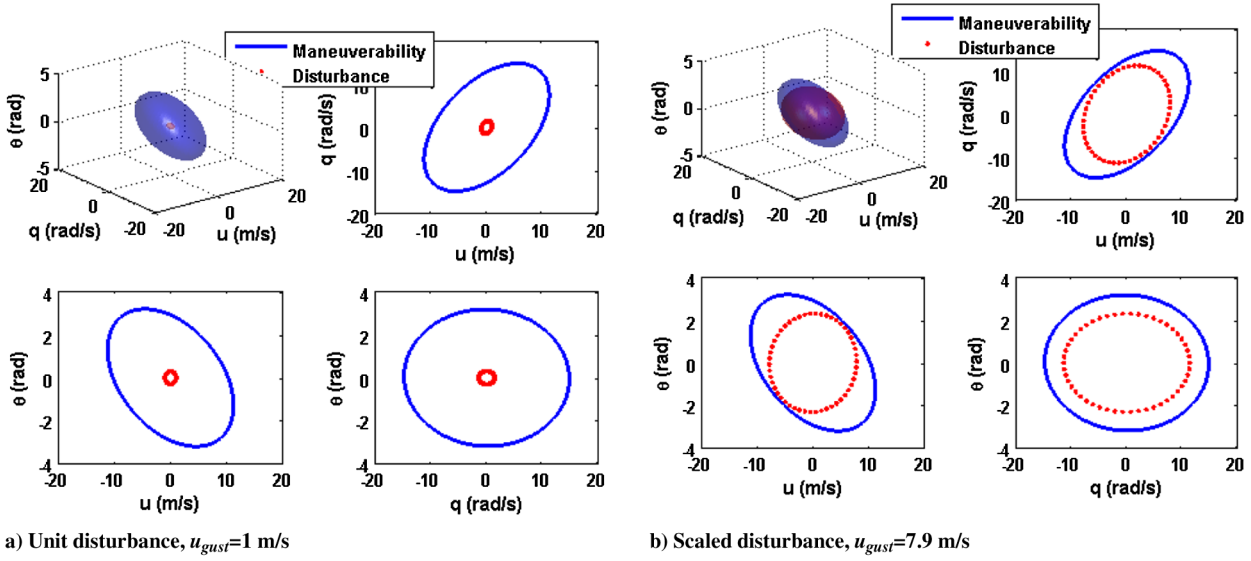


Fig. 30 Maneuverability and disturbance ellipsoids for longitudinal translation gust input.

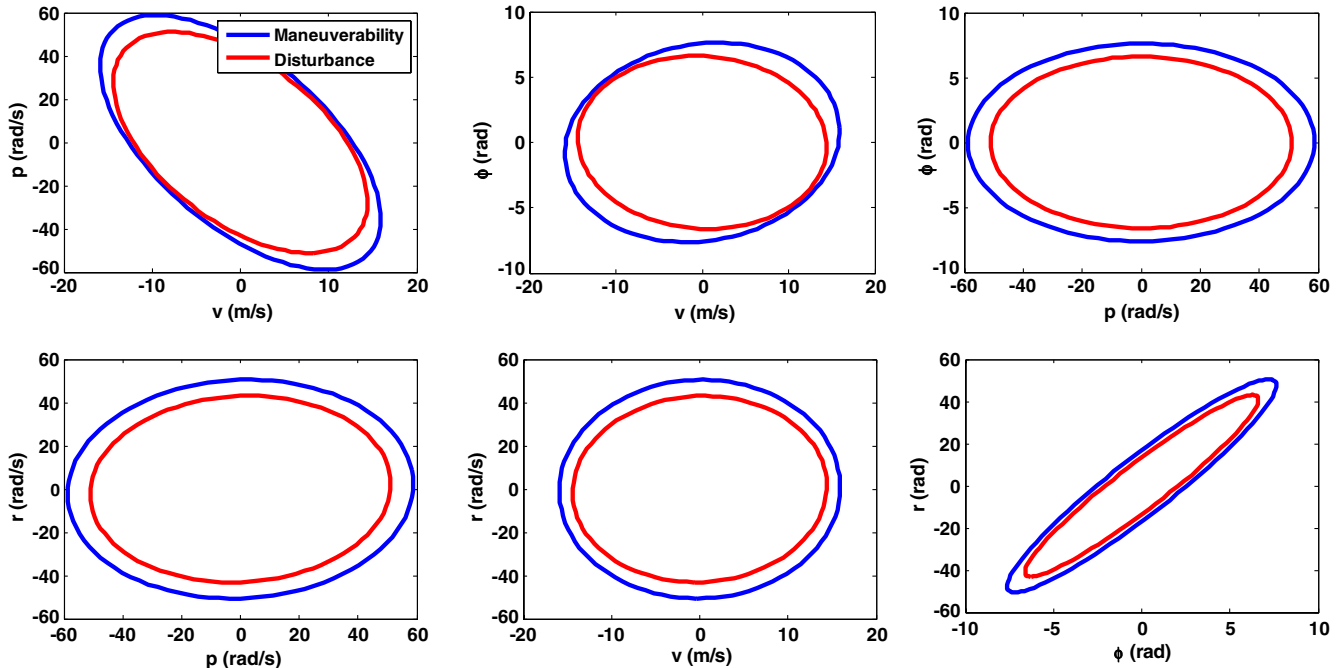


Fig. 31 Maneuverability and disturbance ellipsoid projections for lateral translation gust input.

Now, when the vehicle is subjected to a unit translational gust ($u_{gust} = 1 \text{ m/s}$), the disturbance ellipsoid is computed. It can be seen that the disturbance ellipsoid is completely enclosed by the maneuverability or controllability ellipsoid. As the magnitude of the gust is increased, the volume of the disturbance ellipsoid increases. To extract the maximum translational gust disturbance that the vehicle can overcome, the gust input vector is scaled by a factor such that the disturbance ellipsoid reaches the limit of the maneuverability ellipsoid. As can be seen from Fig. 30b, with a scale factor of about 7.9, one of the projections of the disturbance ellipsoid reaches the limit of the corresponding projection of the controllability ellipsoid. This implies a maximum longitudinal translational gust tolerance of 7.9 m/s.

It is noted that the ellipsoids for the lateral-yaw mode are four-dimensional. Hence, the various projections of these ellipsoids are shown in Fig. 31. It was seen that the maximum value of lateral translational gust that the cyclocopter can tolerate is about 17 m/s. It is interesting to note that the longitudinal translational gust tolerance is much lower than that in the lateral direction. This can be partially

explained by the fact that the restoring forces are larger for the longitudinal direction, which can be deduced from an observation of the stability derivatives X_u , M_u , Y_v , and L_v . Previous wind-tunnel experiments have suggested that, by tilting both the thrust vectors of the cyclorotors into the direction of the wind, the forward flight capability of the vehicle can be enhanced. Analogously, the longitudinal gust tolerance may be enhanced by performing the same.

To obtain a generalized metric for the disturbance rejection capability, the Frobenius norm of the disturbance ellipsoid is computed with a gust input of unit norm ($\|u_{gust}, v_{gust}, p_{gust}, q_{gust}\|$,

Table 6 Frobenius norms for the maneuverability and disturbance ellipsoid

Metric	Value
Disturbance $\ X_D\ _F^{1/2}$	1.8
Scaling α	7.9
Scaled disturbance $\ X_D\ _F^{1/2}$	14.17
Controllability $\ X_C\ _F^{1/2}$	81.8

Table 7 Comparison of translational gust tolerance (in meters per second)

Gust type	Shrouded rotor [12]	Cyclocopter
Longitudinal	3.2	7.9
Lateral	2.4	17

$r_{\text{gust}} \parallel = 1$). It can be deduced that a higher Frobenius norm value of the vehicle for a unit disturbance would imply a lower tolerance to gusts. Now, the gust input vector is scaled up uniformly by a scale factor α . This is determined by the value that results in the disturbance ellipsoid reaching the limits of the maneuverability ellipsoid. The Frobenius norm of the scaled disturbance can then be used as a metric of comparison of gust tolerance. It is evident that the higher the Frobenius norm of the scaled disturbance ellipsoid is, the greater the disturbance rejection capability of the vehicle would be. These values are summarized in Table 6. It is noted that the gust tolerances of the cyclocopter are higher than those estimated for other candidate MAV platforms such as the shrouded rotor [12], which is shown in Table 7.

VII. Conclusions

The present work focused on the flight dynamics identification and analysis of maneuverability and gust disturbance rejection potential of a vertical takeoff and landing capable cycloidal rotor MAV: the twin cyclocopter. The vehicle weighs about 500 g and consists of two optimized cyclorotors set up to spin on the same axis. A tail rotor thrusting in the upward direction is used to balance pitching moment in the aircraft. The vehicle is designed with independent rotational speed control and thrust vectoring capability for each of the cyclorotors.

Systematic input-excitation tests were performed along all degrees of freedom in the closed-loop condition in hover. The flight dynamics model was extracted using time-domain system-identification techniques based on the input-output data. A 6-DOF linear time-invariant dynamic model of the cyclocopter was identified in hover with acceptable identification accuracy ($R^2 > 75\%$ and uncertainty in parameter values of about 10%). It was found that the longitudinal and heave degrees of freedom were decoupled from the rest of the dynamics, whereas the lateral and yaw modes were highly coupled. The lateral and longitudinal stability derivatives, Y_v , L_v , X_u , and M_u were stabilizing. The pitch damping was negative, and pitch attitude dynamics was unstable. Strong gyroscopic coupling between the roll and yaw degrees of freedom were identified from L_r , L_{rud} , N_p , and N_{lon} . This is because both the cyclorotors are spinning in the same direction, which results in a net angular momentum along the spin axis. Any subsequent disturbance would result in a gyroscopic coupled response.

Based on the identified model, the control authority and gust rejection capability of the cyclocopter was then quantified using a control-theoretic framework that characterizes the reachable states of the vehicle for a bounded control and gust disturbance input. This can be useful while comparing the bare airframe capability of the cyclocopter with other MAV platforms in the future. It was seen that the negligible damping in the rate dynamics as well as the presence of the gyroscopic coupling results in a high maneuverability potential of the cyclocopter in open-loop condition. A longitudinal and lateral gust tolerance of 7.9 and 17 m/s were estimated, respectively. This was observed to be significantly higher than a shrouded-rotor MAV (3 m/s gust tolerance) with which the cyclocopter was compared to.

Acknowledgments

This research was supported by the U.S. Army Micro Autonomous System Technologies Collaborative Technology Alliance Center for Microsystem Mechanics with Brett Piekarski (U.S. Army Research Laboratory) and Chris Kroninger (U.S. Army Research Laboratory, Vehicle Technology Directorate) as technical monitors. The authors would like to thank Sean Humbert for his insights and providing the motion-capture facility for testing purposes. The patience and skill of

Shane Boyer for his piloting tasks is greatly appreciated. The authors would also like to thank Elena Shreshta for vehicle troubleshooting and Andrew Kehlenbeck for assisting with setting up the motion-capture system.

References

- [1] McMichael, J. M., and Francis, M. S., "Micro Air Vehicles: Toward a New Dimension in Flight," Aug. 1997, http://www.darpa.mil/tto/MAV/mav_ausvi.html.
- [2] Beekman, D. W., Mait, J. N., and Dogliaski, T. L., "Micro Autonomous Systems and Technology at the Army Research Laboratory," *Proceedings of the National Aerospace and Electronics Conference*, July 2008.
- [3] Hein, B. R., and Chopra, I., "Hover Performance of a Micro Air Vehicle: Rotors in Low Reynolds Number," *Journal of the American Helicopter Society*, Vol. 52, No. 3, 2007, pp. 254–262.
doi:10.4050/JAHS.52.254
- [4] Benedict, M., Ramasamy, M., Chopra, I., and Leishman, J. G., "Performance of a Cycloidal Rotor Concept for Micro Air Vehicle Applications," *Journal of the American Helicopter Society*, Vol. 55, No. 2, April 2010, Paper 022002.
doi:10.4050/JAHS.55.022002
- [5] Benedict, M., Jarugumilli, T., and Chopra, I., "Experimental Investigation of the Effect of Rotor Geometry on the Performance of a MAV-Scale Cycloidal Rotor," *Proceedings of the International Specialists' Meeting on Unmanned Rotorcraft*, Tempe, AZ, Jan. 2011.
- [6] Boirum, C. G., and Post, S. L., "Review of Historic and Modern Cyclogyro Design," *45th AIAA/ASME/SAE/ASEE Joint Propulsion Conference and Exhibit*, AIAA Paper 2009-5023, Aug. 2009.
- [7] Kirsten, F. K., "Cycloidal Propulsion Applied to Aircraft," *Transactions of the American Society of Mechanical Engineers*, Vol. 50, No. 12, 1928, pp. 25–47.
- [8] Hwang, I. S., Hwang, C. P., Min, S. Y., Jeong, I. O., Lee, C. H., Lee, Y. H., and Kim, S. J., "Development of a Four-Rotor Cyclocopter," *Journal of Aircraft*, Vol. 45, No. 6, 2008, pp. 2151–2157.
doi:10.2514/1.35575
- [9] Benedict, M., Gupta, R., and Chopra, I., "Design, Development and Flight Testing of a Twin-Rotor Cyclocopter Micro Air Vehicle," *Proceedings of the 67th Annual National Forum of the American Helicopter Society*, Virginia Beach, VA, May 2011.
- [10] Benedict, M., Shreshta, E., Hrishikeshavan, V., and Chopra, I., "Development of 200 Gram Twin-Rotor Micro Cyclocopter Capable of Autonomous Hover," *Proceedings of the American Helicopter Society Future Vertical Lift Aircraft Design Conference*, San Francisco, Jan. 2012.
- [11] Humbert, J. S., and Faruque, I., "Analysis of Insect-Inspired Wingstroke Kinematic Perturbations for Longitudinal Control," *Journal of Guidance, Control, and Dynamics*, Vol. 34, No. 2, 2011, pp. 618–622.
doi:10.2514/1.51912
- [12] Hrishikeshavan, V., Humbert, S., and Chopra, I., "Controllability and Disturbance Gramian Analysis of a Shrouded Rotor MAV in Hover," *Proceedings of the American Helicopter Society Specialists' Meeting for Unmanned Rotorcraft*, Jan. 2013.
- [13] Mehta, A., and Pister, K., "WARPWING: A Complete Open Source Control Platform for Miniature Robots," *2010 IEEE/RSJ International Conference on Intelligent Robots and Systems (IROS 2010)*, IEEE Publ., Piscataway, NJ, Oct. 2010, pp. 5169–5174.
- [14] Tischler, M. B., and Remple, R. K. *Aircraft and Rotorcraft System Identification*, AIAA Education Series, AIAA, New York, 2006, pp. 90–92.
- [15] Morelli, E. A., "System Identification Programs for Aircraft (SIDPAC)," *AIAA Atmospheric Flight Mechanics Conference*, AIAA Paper 2002-4704, Aug. 2002.
- [16] Morelli, E. A., "Practical Aspects of the Equation-Error Method for Aircraft Parameter Estimation," *AIAA Atmospheric Flight Mechanics Conference and Exhibit*, AIAA Paper 2006-6144, Aug. 2006.
- [17] Dullerud, G. E., and Paganini, F. *A Course in Robust Control Theory*, Vol. 6, Texts in Applied Mathematics, Springer, New York, 2000, pp. 150–153.
- [18] Zhou, K., Salomon, G., and Wu, E., "Balanced Realization and Model Reduction for Unstable Systems," *International Journal of Robust and Nonlinear Control*, Vol. 9, No. 3, 1999, pp. 183–199.
doi:10.1002/(SICI)1099-1239(199903)9:3<183::AID-RNC399>3.0.CO;2-E
- [19] Nelson, R. C. *Flight Stability and Automatic Control*, McGraw-Hill, New York, 1989, pp. 180–183.